Design criteria for selective nanofluidic ion-exchange membranes

Petrov, Kostadin V.; Santoso, Albert; Ryzhkov, Ilya I.; Vermaas, David A.

DOI
10.1016/j.memsci.2023.122156

Publication date
2023

Document Version
Final published version

Published in
Journal of Membrane Science

Citation (APA)
Petrov, K. V., Santoso, A., Ryzhkov, I. I., & Vermaas, D. A. (2023). Design criteria for selective nanofluidic ion-exchange membranes. *Journal of Membrane Science*, *688*, Article 122156. https://doi.org/10.1016/j.memsci.2023.122156

Journal of Membrane Science 688 (2023) 122156

Contents lists available at ScienceDirect

Journal of Membrane Science

journal homepage: www.elsevier.com/locate/memsci

Design criteria for selective nanofluidic ion-exchange membranes

Kostadin V. Petrov [a,**], Mark Mao [a], Albert Santoso [a], Ilya I. Ryzhkov [b,c], David A. Vermaas [a,*]

[a] Department of Chemical Engineering, Delft University of Technology, 2629 HZ, Delft, the Netherlands
[b] Institute of Computational Modeling SB RAS, Akademgorodok 50-44, 660036, Krasnoyarsk, Russia
[c] Siberian Federal University, Svobodny 79, 660041, Krasnoyarsk, Russia

ARTICLE INFO

Keywords:
Ion-exchange membrane
Nanofluidic
Nanopore
Permselectivity
Inorganic membrane

ABSTRACT

Polymeric ion-exchange membranes (IEMs) are key to many electrochemical processes, but their intrinsic selectivity limitations restrict scale-up possibilities. Nanofluidic IEMs, based on inorganic rigid materials and charged nanopores, offer a promising alternative. We present design criteria for selective nanofluidic membranes. We used commercial anodized aluminium oxide (AAO) membranes with varying pore sizes to measure permselectivity between different KCl concentrations. Our experiments reveal that membranes with 10-nm pores have permselectivities above 90%, comparable to those of polymeric IEMs, up to electrolyte concentrations of 0.15 vs. 0.75 M. To our knowledge, this is the highest reported ion selectivity for nanofluidic IEMs. Conversely, asymmetric AAO membranes featuring a thin selective layer, exhibited low permselectivity. We explored the influence of other parameters through simulations using the space-charge model. Our numerical results indicate that pore size and surface potential are the most sensitive parameters for increasing selectivity. Additionally, pore length has a minimum requirement for good performance although increasing it beyond the μm scale yields no significant result. This study highlights nanofluidic IEMs as a promising alternative to polymeric IEMs and their capability to improve performance of many electrochemical processes, especially those involving low electrolyte concentrations on at least one membrane side.

1. Introduction

Depletion of drinking water across dry regions and the global energy transition toward renewable sources has boosted the relevance of electrochemical processes aimed at water treatment, energy storage, and energy conversion [1–3]. Examples of emerging or industrially established processes include electrodialysis (ED) [4–6], ion-exchange membrane bioreactors [7], reverse electrodialysis (RED) [8,9], fuel cells [10,11], redox flow batteries [12,13], the chlor-alkali process [14], and water and CO_2 electrolysis [15–17]. In all these processes, ion-exchange membranes (IEMs) are key components because of their selective ion conductivity.

The vast majority of IEMs are based on a polymeric matrix with immobilized charged functional groups [18]. These groups are responsible for the Donnan effect, rejecting ions with the same charge (co-ions) and allowing oppositely charged ions (counter-ions) to permeate [19]. Yet there is a conductivity-to-selectivity trade-off. This arises from challenges related to the flexible polymeric backbone and charged functional groups, such as swelling [20,21], which leads to free water volume inside the matrix and limits the density of immobilized charges. Volume in the polymeric matrix grows with increasing degree of functionalization, which increases conductivity but decreases selectivity [22,23]. Since most IEMs have a charge density of 0.5–3 M, polymeric IEM selectivity is very limited in high electrolyte concentrations [24–27]. Many IEMs with sufficient conductivity have selectivity around 90% at 1 M electrolyte concentrations. This limits their potential usage for applications that, for example, employ brine solutions, such as power generation via RED [28]. The trade-off between membrane selectivity and conductivity as well as the intrinsic limits in charge density hamper improvement of traditional IEMs [3,29–34]. Additionally, polymeric IEMs suffer from steric hindrance, leading to a relatively high resistance to ion transport [35], and ageing due to chemical degradation in harsh environments [36,37].

Nanofluidic membranes (NFMs) are alternative IEMs whose selectivity mechanism does not rely on charged functional groups, but on the surface charge within the nanopore [38–40]. The radii of these nanopores is close in magnitude to the thickness of the electrical double layer (EDL). Therefore, the EDL covers the majority or the entirety of the

* Corresponding author.
** Corresponding author.
E-mail addresses: k.v.petrov@tudelft.nl (K.V. Petrov), d.a.vermaas@tudelft.nl (D.A. Vermaas).

https://doi.org/10.1016/j.memsci.2023.122156
Received 2 August 2023; Received in revised form 23 September 2023; Accepted 7 October 2023
Available online 8 October 2023

nanopore, charging the fluid inside. This allows the NFM to reject co-ions and allow counter-ions to permeate; the NFM hence functions as an IEM [41]. Based on rigid materials without swelling issues, NFMs offer new possibilities in chemical stability and can be made ultrathin, thus enhancing ionic conductance.

Various fields apply single charged nanopores, such as nanofluidics and biosensing [42,43], but sheets with a large nanopore density, such as NFMs, have only recently been used for power generation [41]. The main reason is that most nanoporous materials are not easily scalable [38]. They have been produced using techniques such as focused ion beam [44,45], electron beam [35], and ion-track etching [46,47], none of which yet exist on a commercial scale [38]. Moreover, nanofluidic IEMs are a novel concept; as such, we lack understanding of how different parameters affect their selectivity.

Anodic aluminium oxide (AAO) is a commercially available material that can be produced with different pore geometries. It has a considerable surface charge even at neutral pH and perfectly arrayed cylindrical pores with a high pore density [48,49]. Being one of the few materials that combines these properties, it is widely studied, but selectivities that can compete with polymeric IEMs have so far not been achieved. Kim et al. [50] achieved an apparent permselectivity of ~60% by fabricating wide slits with a 4-nm height, while Kim et al. [51] achieved similar selectivity values using cylindrical pores with a 20-nm diameter. Using an asymmetric AAO membrane with two different pore diameters – the smaller being 2 nm – Lee et al. [52] achieved a permselectivity of approximately 100% at very low electrolyte concentrations, with a sharply decreasing selectivity with increasing concentration. These results, along with those documented in previous literature [53], prove that pore geometry greatly impacts counter-ion selectivity of these membranes. Additionally, it is important to note that extrapolating existing findings from single nanochannels to NFMs might not be straightforward due to other potential factors, such as concentration polarization. Despite theory suggesting that lower pore diameter should increase selectivity, controlling pore size is challenging when dealing with very small pores. Optimization of NFM pore geometry is therefore essential to achieve peak performance in practical fluid applications.

This article aims to elucidate design criteria for inorganic nanoporous IEMs and investigate, both experimentally and numerically, to what extent AAO sheets can act as selective IEMs. For this study, we used commercial AAO membranes with different pore sizes to experimentally determine their permselectivity and simulated further parameters using the space-charge model (SCM). Our results suggest that these membranes can compete with polymeric IEMs in terms of permselectivity.

2. Background

The EDL is the ionic structure formed in the vicinity of a charged surface when immersed in an electrolyte. The electrochemical potential that arises at the solid-liquid interface causes the structure to form. It comprises two layers: the Stern layer, which is compact and very close to the surface, where ions are typically stagnant or have a very reduced mobility; and the diffuse layer, in which the concentration of counter-ions exponentially decreases in function of the distance to the surface until it reaches the bulk concentration [54]. Within the EDL, there is no electroneutrality as the counter-ion species is present in much higher concentration than the co-ion. The EDL thickness is characterized by the Debye length (λ_D), expressed as:

$$\lambda_D = \sqrt{\frac{\varepsilon_r \varepsilon_0 R_g T}{2 \cdot 10^3 F^2 C_B}} \tag{1}$$

where ε_r is the relative permittivity, ε_0 is the permittivity of free space (F/m), R_g is the gas constant ($Jmol^{-1}K^{-1}$), T is the absolute temperature (K), F is the Faraday constant (C/mol), and C_B is the bulk electrolyte concentration (mM) [55]. Since λ_D depends on the bulk concentration (**Equation (1)**), high selectivities can be achieved with low concentrations or narrower pores.

Evidence also shows that selectivity is determined by the Dukhin number (Du), rather than the Debye length. The Dukhin number (**Equation (2)**) is the ratio between the surface conductivity induced by the charge on the pore walls and the bulk conductivity, which can be simplified as:

$$Du = \frac{|\sigma|}{F C_B R_p} \tag{2}$$

where σ is the surface charge density (C/m^2) and R_p is the pore radius (m) [56,57]. The increased concentration of ions in the EDL, close to the surface, leads to an increased conductivity in this part of the solution. This effect is called surface conductance [58]. When a driving force is applied across the membrane, ion transport occurs through the most conductive regions, which is the vicinity of the charged walls (the EDL), especially when the bulk concentration is low. This explains selectivities observed for pore sizes larger than the Debye length and the relationship between surface charge density and selectivity [44,51]. A Du $>$ 1 indicates ionic selectivity for the nanopores [56].

It is notable that the surface charge density itself can vary according to the environment. This depends on a material's surface potential, which in turn is dependent on the pH and on the electrolyte concentration [59]. The Grahame equation provides a relationship between the surface potential at the pore wall and the surface charge density as [60]:

$$\sigma = \sqrt{8 C_B \epsilon \epsilon_0 k_B T} \sinh \frac{z e \varphi_0}{2 k_B T} \tag{3}$$

where ϵ is the permittivity of the solution (78.4 for water), ϵ_0 is the vacuum permittivity (8.854×10^{-12} F/m), k_B is the Boltzmann constant (1.381×10^{-23} J/K), z is the ion valence, e is the elementary charge, and φ_0 is the pore wall potential. Since no transport occurs in the Stern layer, the ζ potential is used as a boundary condition for surface potential (φ_0) and ion transport calculations [60].

Although Du gives a good indication of the membrane's selectivity, more complex situations (such as distinct electrolyte concentration on either side) are usually solved using numerical simulations. Ion transport in nanochannels is often described by the space-charge model, initially developed by Morrison and Osterle [61]. This model considers a single nanopore, assuming an axisymmetric cylinder of length L and radius R_p, with x being the axial (longitudinal) coordinate and r being the radial coordinate. The pore connects two reservoirs of electrolytes with different concentrations, C_{low} and C_{high}. The pressure in the reservoirs is equal. Ion flux (J_i) is described by the Nernst-Planck (NP) equation as:

$$J_i(x,r) = c_i(x,r)u(x,r) - D_i \nabla c_i(x,r) - D_i \frac{z_i c_i F}{R_g T} \nabla \varphi(x,r) \tag{4}$$

where u is the velocity of the fluid (m/s), D_i is the diffusion coefficient of the ion species i (m^2/s), z_i is the valence of ion i, and φ is the electrical field (V). The first term on the equation's right hand-side describes convective flow, the second accounts for diffusion, and the last accounts for migration. Electrical field and concentration profiles are described by the Poisson-Boltzmann (PB) equation as:

$$\nabla^2 \varphi = -\frac{\rho_e}{\epsilon \epsilon_0} = -\frac{F}{\epsilon \epsilon_0}(c_+(x,r) - c_-(x,r)) \tag{5}$$

where ρ_e is the charge density (C/m^3) within the pore. To simplify the model, it is often assumed that local equilibrium is present in the radial direction (r) since the pore is much longer than its width. This leads to the assumption that ion flux and fluid velocity in the radial direction are 0. This allows us to insert Equation (5) into the r-component of Equation (4), which results in:

$$\frac{\partial c_i(x,r)}{\partial r} = -\frac{z_i c_i(x,r) F}{R_g T} \frac{\partial \varphi_r(x,r)}{\partial r} \tag{6}$$

This can be integrated into the Boltzmann distribution as:

$$c_i(x,r) = c_v(x)\,\exp\left(-\frac{z_i F}{R_g T}\,\varphi_r(x,r)\right) \tag{7}$$

We use the subscript *v* to represent "virtual" quantities expressing the principle of local equilibrium.

These equations can be solved using the boundary conditions of fixed wall potential and considering the cylindrical symmetry as:

$$\varphi_r(x,R_p) = \varphi_0 - \varphi_v(x) \tag{8}$$

$$\frac{\partial \varphi_r(x,0)}{\partial r} = 0 \tag{9}$$

where φ_0 is the potential at the pore wall, for which we used the ζ-potential value.

Finally, the velocity profiles within the pore can be obtained by the Navier-Stokes (NS) equation as:

$$\mu\nabla^2 u(x,r) - \nabla p_h(x,r) - \rho(x,r)\nabla\varphi(x,r) = 0 \tag{10}$$

$$\nabla \bullet u(x,r) = 0 \tag{11}$$

where μ is the viscosity (Pa.s) and p_h is the hydrostatic pressure (Pa). The boundary conditions for velocity involve assuming a no-slip boundary condition and that the wall is impermeable to both fluids and ions, expressed as:

$$u(x,R_p) = 0 \tag{12}$$

The governing equations of the space-charge model (Equations (4), (5) and (10), and 11) are highly coupled to each other, making it very complicated to solve even for simple geometries [62]. Consequently, the solution is typically obtained through numerical methods.

3. Methods

3.1. Permselectivity experiments

A two-compartment setup (Fig. 1a) allowed us to experimentally measure the permselectivity of a membrane. We placed a membrane between two compartments (150 mL each) of electrolyte solutions with different concentrations and then measured electrical potential difference between them using two double-junction Ag/AgCl reference electrodes connected to an Autolab PGSTAT 128 N potentiostat (Metrohm, Switzerland). The tested membranes were AAO discs with a diameter of 1.3 ± 0.1 cm and an array of straight cylindrical nanopores of different pore sizes (InRedox, Colorado, USA), which act as an anion exchange membrane at neutral pH. We tested two sets of membranes: symmetric membranes with pore sizes of 10, 20, and 50 nm (in diameter); and asymmetric ones with a 150-nm pore size throughout the majority of the membrane thickness, and a 1.5-μm thick selective layer with a branched structure with a pore size of 3 ± 2 nm or 5 ± 2 nm (Fig. S1). The membranes were used as delivered without any pre-treatment. We placed the membranes in a holder between two flat O-rings, leaving 0.64 cm^2 of open area, which we then placed between the two electrolyte compartments. KCl was our chosen electrolyte for these measurements because K^+ and Cl^- ions have approximately the same mobilities, and therefore the measured potential is not affected by diffusion potentials – only the Donnan potential would be detected. 500 mL of electrolyte were used to reduce the potential impact of concentration changes. The electrolyte in the compartments was kept flowing at 40 mL/min using a peristaltic pump to minimize concentration polarization. To avoid pH changes due to CO_2 dissolution from the air during the experiment, we bubbled a small amount of N_2 gas in the electrolyte reservoirs. Before measuring membrane potential, we kept the solutions flowing for at least 3 h to ensure equilibration with the membrane. The potential was then taken as an average of at least 120 s. After obtaining three measurements, we rinsed and swapped the reference electrodes and took three more measurements. By averaging the six measurements, we ensured no effect of possible drift of the potential of the reference electrodes. We obtained the activity coefficients using Visual MINTEQ 3.1 software. The Cl^- concentrations in the two compartments were measured right after the experiment using an 881 IC pro ion chromatograph with a 150-mm A Supp 5/4.0 column (Metrohm, Switzerland). These concentrations were then used to calculate the Nernst potential.

An adapted version of the Nernst equation (Equation (13)), which can be written for a 1:1 salt, and the measured membrane potential (E_M) enabled us to obtain the transport numbers within the membrane: t_-^m and t_+^m for counter-ions (anions) and co-ions (cations), respectively. The equation can be expressed as:

$$E_M = \frac{RT}{F}\left(t_-^m - t_+^m\right)\ln\frac{a_1}{a_2} \tag{13}$$

Where a_1 and a_2 are the activities of the ions in the two compartments. If the transport number for counter-ions is 1, then the equation just equals the classical Nernst equation, which would be our ideal measured potential (E_{M_ideal}). We calculated the apparent permselectivity as follows:

$$\varphi = \frac{\frac{E_M}{E_{M\_ideal}} + 1 - 2t_i}{2t_j} \approx \frac{E_M}{E_{M\_ideal}} \tag{14}$$

where t_i and t_j stand for the transport numbers in the bulk of counter-ions and co-ions, respectively. In this case, they are approximately the same since KCl was used as the electrolyte.

3.2. Membrane characterization

To characterize surface morphology, we used focused ion beam

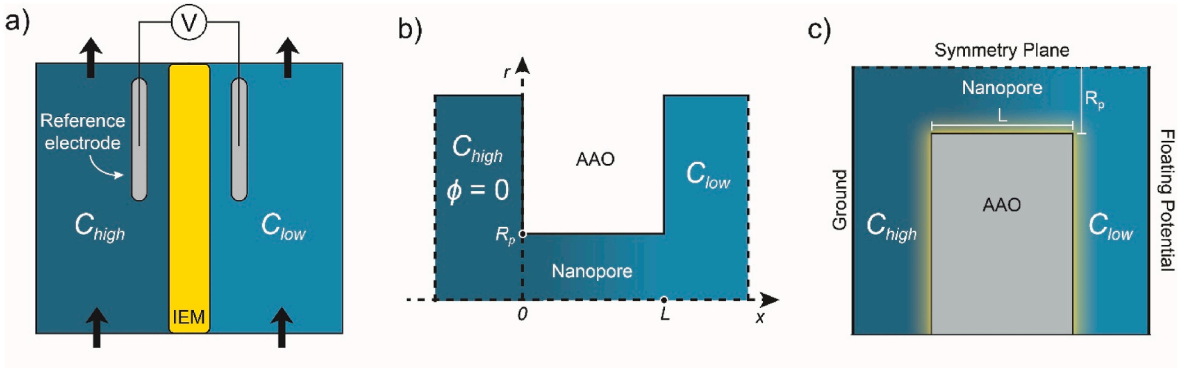

Fig. 1. a) A schematic shows the permselectivity setup. b) The geometry modeled in the ITM software. c) The geometry modeled in COMSOL Multiphysics.

scanning electron microscopy (FIB-SEM, FEI Helios G4 CX). Since this tool requires a conductive surface, we deposited gold nanoparticles on the AAO samples. We used 30 s of deposition time for imaging and 300 s for FIB cutting. The image was obtained using three different detectors, depending on the best-obtained contrast: an Elstar in-lens secondary electrons detector (TLD-SE), an Everhart-Thornley detector (ETD), and a high-performance ion conversion detector (ICE) at a beam current of 18–86 pA and electron energy of 10–30 keV. A complementary image was obtained using field emission scanning electron microscopy (FESEM, Hitachi Regulus SU8230) at a beam current of 1–5μA and electron energy of 10–15 keV. We used the FIB for cutting a part of the sample to observe the cross-section with transmission electron microscopy (TEM). A JEOL JEM 3200FS microscope enabled us to obtain the TEM images at 150,000x magnification.

Image-processing the microscopy pictures enabled us to make pore size distributions from both TEM and SEM analysis. Further details on the image-processing methodology are available in the supporting information (SI) (Figs. S2–S3).

Using TriStar II 3020 equipment (Micromeritics), we measured nitrogen adsorption-desorption isotherms at 77 K. Before the analysis, we degassed 23 mg of AAO material under vacuum at 250 °C for 16 h. The Brunauer–Emmett–Teller (BET) surface area of the membranes was measured at 46.06 ± 0.08 m^2/g. The Barrett, Joyner, and Halenda (BJH) method for the desorption cumulative volume of the pores up to 300 nm showed a volume of 0.252 cm^3/g. We fit these cumulative curves to obtain a pore size distribution by having incremental volumes at even steps and correcting this volume to obtain a relative frequency of each pore size interval (see Fig. S4).

We also measured the water permeability of our membranes, but the permeability of the AAO membranes was too low to accurately measure. Details can be found the supporting information (Fig. S5).

3.3. Simulations

The fourth author of this article, professor Ilya Ryzhkov, developed a software called Mathematical Modelling of Ion Transport in Membranes (ITM software) [53,63]. The software numerically solves the space-charge model, which describes the ion-transport through cylindrical nanopores with a known surface potential. The pores connect two electrolyte tanks (Fig. 1b) and permit inclusion of a Stern layer and a diffusion boundary layer outside the pores. In our simulations, pore size, pore length, electrolyte concentration, and surface potential were varied while remaining parameters were kept constant (see Table S1). Unlike with other models, the ITM software allowed us to use a constant surface potential (instead of surface charge density) as a boundary condition. Pore size was kept above 3 nm because below that value, the continuum assumption becomes questionable [56]. The diffusion coefficients for K^+ and Cl^- were taken as 1.957×10^{-9} m^2/s and 2.032×10^{-9} m^2/s, respectively. Fluid viscosity was 0.888×10^{-3} Pa s. The temperature was 298.15 K. For the entirety of the nanopore, we used the relative permittivity of water, taken as 78.49. The boundary condition used for surface potential in the modeling was the ζ potential, which is measured at the shear plane of the EDL [64]. Therefore, the pore size was corrected after the modeling to include the Stern layer thickness which was considered to be 0.5 nm. The effective pore size for ion transport is 1 nm smaller than what is reported in our simulation results.

Another model was created in COMSOL to assess the effect of the surface around the entrance of the nanopore, which was not possible to do with the ITM software. The COMSOL model used the Poisson-Boltzmann and Nernst-Planck equations in a 2D axy-symmetrical geometry (Fig. 1c) with four domains: two electrolyte tanks with defined concentration on the edge farther from the membrane; a membrane with a specific surface potential and no ion-flow across the walls; and a channel under the influence of this surface charge connecting the two reservoirs. The simulations evaluated the effect of including or not including the surface of the membrane, as opposed to solely applying the boundary conditions to the pore walls.

4. Results and discussion

4.1. Permselectivity experiments

We measured the apparent permselectivity of different IEMs between two compartments with different KCl concentrations. Fig. 2a shows the apparent permselectivity vs. concentration at a fixed concentration ratio C_{low}:C_{high}, of 1:5. The general trend of decreasing selectivity for higher electrolyte concentration was expected from the Donnan equilibrium theory. The AAO selectivity was benchmarked against two polymeric membranes: Selemion AMV, developed for electrodialysis and one of the most selective commercial anion exchange membranes [65], and Sustainion X37, geared for electrolysis [66]. Fig. 2a shows that the AAO membrane with 10-nm pores had an apparent permselectivity of above 90% and was comparable with Selemion AEMs up to concentrations of approximately 0.7 M. Although its permselectivity rapidly decreased after this value, it was considerably more permselective than Sustainion in the whole concentration range. To our knowledge, this the highest permselectivity reported for NFMs.

The AAO membrane with 20-nm pores had a permselectivity comparable to that of Sustainion membranes, with an 80% permselectivity at 5 mM, which decreases with increasing concentration. The membranes with 50-nm pores showed poor selectivity, below 50% for the entire tested concentration range. This further evidenced the relationship between pore size and selectivity, where higher permselectivities are observed at lower pore sizes.

Finally, the anisotropic AAO membranes, which have a thin selective layer (1.5 μm thickness) of 3 ± 2-nm or 5 ± 2-nm pores on top of a support layer with 150-nm pores, also exhibited a poor permselectivity, comparable to that of a membrane with 50-nm pores. We hypothesize that the limited pore length of the fine pore layer caused the poor selectivity. Additionally, since diffusion flux is inversely proportional to thickness, a more pronounced concentration polarization was present, notably internally – in the section with 150-nm pores. Concentration polarization due to diffusion resulted in a lower concentration gradient over the membrane. The results in Fig. 2a suggest that a certain pore length is required to achieve high selectivities. These samples have a branched type of structure at the end (Fig. S1), whereby narrow pore size is achieved for a very limited length. This shows that the branched structure was not enough to establish a selective layer, thereby urging further study of the effect of pore length (see Simulations section).

Fig. 2b displays the apparent permselectivity of an AAO membrane with 10-nm pores for different concentrations and ratios of concentrations. The results showed that for all ratios, there was a decrease in permselectivity for increased concentration. Permselectivity was higher for higher ratios in concentrations when plotted against the C_{high}. When plotted against the C_{low}, we observed the opposite effect (Fig. S6). Both concentrations on the two sides of the membrane therefore had an effect on selectivity.

To better understand the high permselectivities for AAO membranes with 10-nm pores and the potential for further tuning its properties, we thoroughly characterized the membranes and built a model explaining the relationship between pore geometry, the different parameters, and permselectivity.

4.2. Membrane characterization

Fig. 3a shows the SEM image of the surface of the AAO membrane with 10-nm pores. The membrane has a highly ordered, dense array of pores of similar size. These properties deem it suitable to function as an IEM. Fig. 3b shows the TEM image of the same membrane's cross-section. At the top of the figure, a darker area with circular shapes represents the gold nanoparticles deposited for the FIB cut that prepared the sample for TEM. The figure's lighter middle section shows the

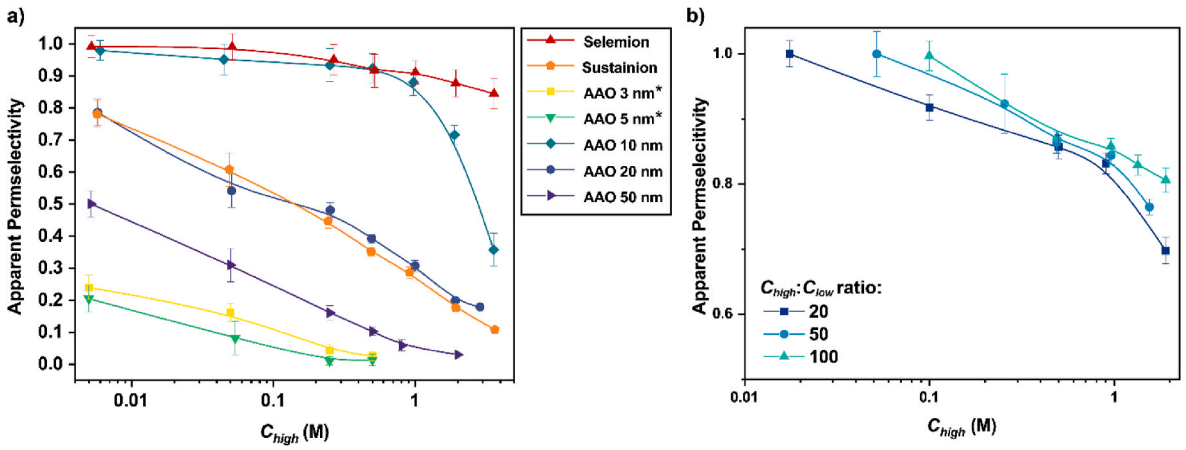

Fig. 2. a) Apparent permselectivity of two polymeric IEMs – Selemion AMV and Sustainion X37 – and five AAO membranes with different pore sizes (3–50 nm) placed between two reservoirs with a concentration ratio of 5.*3-nm and 5-nm pores are asymmetric membranes with only a thin selective layer. b) Apparent permselectivity results showcase the effect of concentration and concentration ratio on permselectivity of the AAO membrane with 10-nm pores. Note that the figures have different scales.

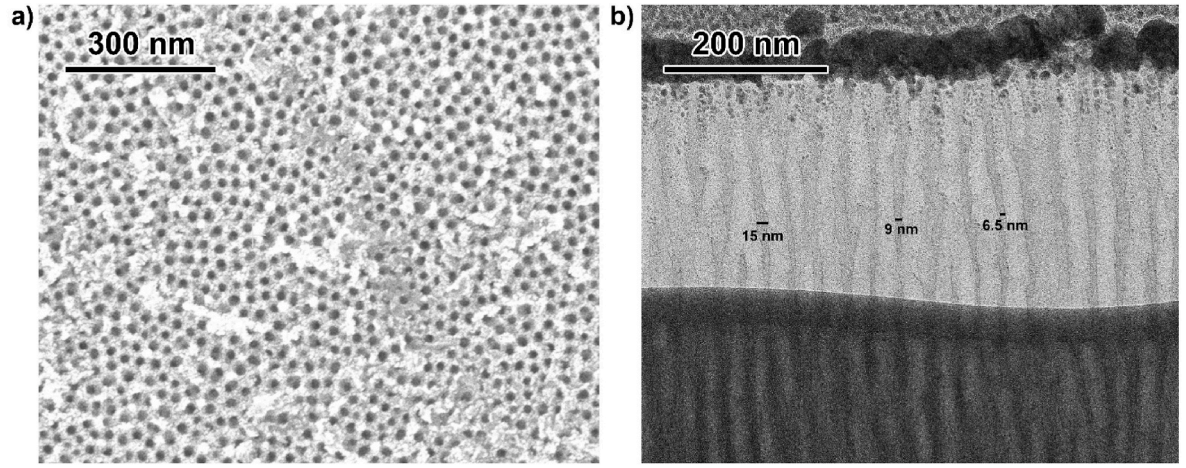

Fig. 3. a) A SEM image of the AAO membrane surface shows a 10-nm pore at 120,000x magnification. b) A TEM image shows a cross-section of the same membrane at 150,000x magnification; nanopore morphology can be observed in the light gray area in the middle portion of the figure.

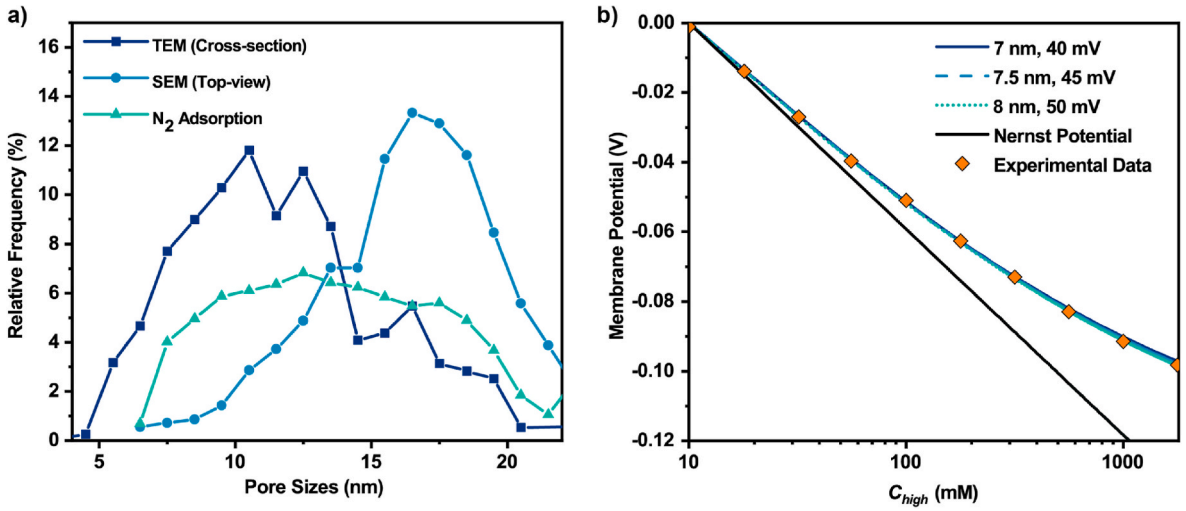

Fig. 4. a) Pore size distributions are shown. b) Membrane potential data is fit with the ITM software. The three lines have a combination of pore sizes of 7, 7.5, and 8 nm and 40, 45, and 50 mV of ζ potential.

nanopores, which do not appear to be perfectly cylindrical; they sometimes narrow or widen and at some points converge and diverge, causing a wider pore size distribution than expected. We can also observe how the pores often widen at the top, giving them a slightly funneled shape (Fig. S7).

Fig. 4a shows the size distribution on the AAO membrane with 10-nm pores determined by three different methods. All methods resulted in a wider pore size distribution than expected or provided by the supplier. Since the pores slightly widen at the top (Fig. 3b and Fig. S7), the entire distribution curve determined by SEM is shifted toward larger pore sizes. On each of the membrane's two sides (see Figs. S8 and S9), we also observe a different morphology and perhaps even a different pore density. This further explains the large pore size distribution. Average pore size determined by treating the TEM data is 10.6 ± 3.5 nm; by fitting the nitrogen desorption curve, the average pore size obtained was determined at 13.5 nm. However, because the larger pore size (near the surface) and narrow pore size (in the middle) were connected in series, we expected the narrower parts to determine the membrane's selectivity. Because the TEM data showed pore sizes starting at 5 nm and an average pore size of roughly 10 nm, we expected the effective pore size for determining the selectivity in these samples to be somewhere between 5 and 10 nm.

To further elucidate the effective pore size and understand the experimental results, we compared the experiments with simulated values from the ITM software. For model validation over a broad range in membrane potential, we performed a new set of permselectivity experiments keeping C_{low} at 10 mM while increasing C_{high} stepwise. According to the literature, the ζ potential of an AAO surface in aqueous solutions ranges between 40 and 50 mV at neutral pH, depending on the electrolyte concentration [59,67,68]. Fig. 4b shows the comparison of the experimentally obtained membrane potential values with simulation data. Combinations of pore sizes between 7 and 8 nm and ζ potentials between 40 and 50 mV were shown to fit the experimental data perfectly. For the remaining simulations, we used 7 nm as the pore size and 40 mV as the surface potential boundary condition.

We observed that the experimental data fit remarkably well when using a constant membrane potential. Using a constant surface charge density instead (Fig. S10) did not yield good fits; this was because the surface charge density depended on the electrolyte concentration, which vary along the length of the pore, especially when the membrane is between two solutions of different concentrations [60]. This shows the simulations can accurately predict the selectivity of AAO when using constant membrane potential.

It is important to note that although the simulation perfectly fit the experimental data using C_{low} = 10 mM, shown in Fig. 4b, it failed at higher concentrations for the samples labeled 10 nm (and with effective pore size of 7 nm) (Fig. S11). This discrepancy was even more pronounced at low concentration ratios (Fig. S12). To some extent, experimental data was subject to sample-to-sample variation, not least because of the broad pore size distribution. ζ potential could also vary along the pore, notably at the elevated electrolyte concentrations at low ratios [59]. Pore size and length also determined the diffusion flux through the pore and therefore influenced the concentration polarization, which was not taken into account by the model. Nevertheless, since the simulations were consistent with a large portion of the experimental data, they were considered a useful tool to further explore the concept of nanofluidic IEM selectivity.

4.3. Simulations

In order to explain the relationship between membrane properties and operating conditions, we used the ITM model to simulate the effect of these parameters. This model enabled simulation of different membrane properties and operation conditions that were not possible to verify experimentally and offered further insight into the executed experiments.

Firstly, to gain deeper insight into the selectivity mechanism, we plotted the simulated ion concentration profiles within a nanopore. Fig. 5a and b show the longitudinal and radial ion profiles, respectively. Fig. 5a shows a jump in ion concentration occurring at the entrances of the pore, together with a sudden jump in Donnan potential (Fig. S13a). The pronounced jump is partly due to the SC model's use of jump boundary conditions. In a real scenario, the electric field increases more progressively, which can only be captured by a model with continuous change of potential and ion concentration at the interfaces. Nevertheless, when such a model is used, although smoother, a pronounced jump in potential and concentration is still observed at the interfaces [53]. Since the surface potential is positive, the concentration of anions inside the pore is higher than in the bulk. Concentration and surface charge density (Fig. S13b) inside the nanopore vary almost linearly along the length of the pore (from $z = 0$ to $z = L$). The jump in potential and concentration suggests that the selectivity is mainly created by these interfaces. The largest counter to co-ion ratio is observed a $z/L = 1$, which suggests this interface plays a significant role in the selectivity.

The radial profiles (Fig. 5b) show that the largest ion concentrations are close to the pore wall, with counter-ion concentration exceeding co-

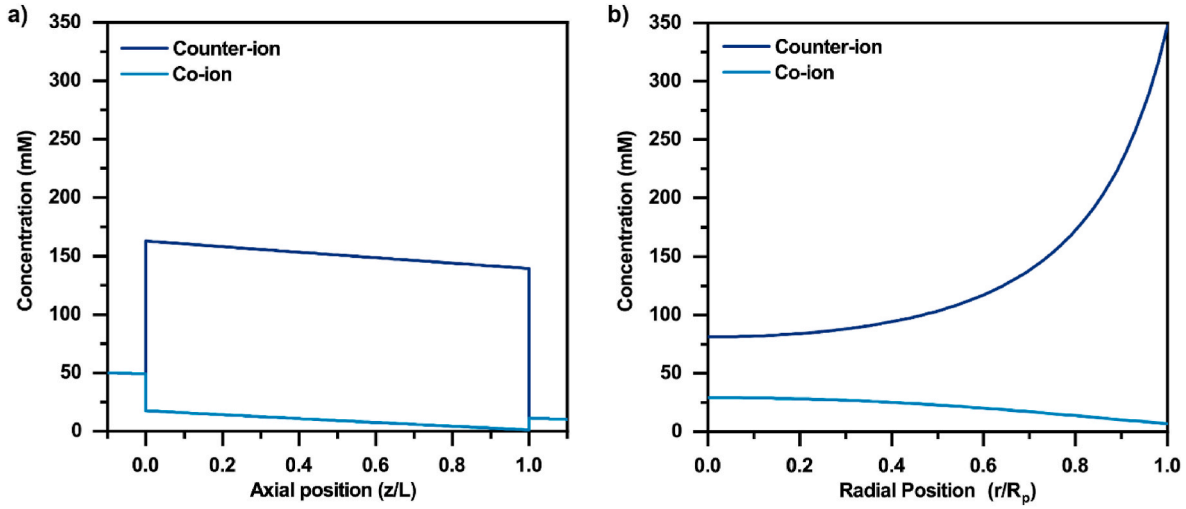

Fig. 5. Ion concentration profiles inside a pore with a 7-nm diameter (effective R_p = 3 nm) and a 1-μm length are shown placed between two reservoirs with 10 mM and 50 mM of KCl. a) Longitudinal ion concentration profiles are shown with averaged concentration at each z position. b) Radial ion concentration profiles are shown at z/L = 0.5, where 0 is the center of the pore and 1 is the pore wall.

ion concentration even in the center of the pore. This shows that the entirety of the nanopore has a certain degree of selectivity even though there is no EDL overlap at this concentration. Moreover, both the highest conductivity and highest counter-/co-ion separation were observed close to the pore wall. This provides evidence for the surface conductance mechanism described earlier. The high counter-ion concentration close to the pore wall also clarifies that higher selectivities can be achieved with smaller nanopores.

To investigate the relationship between pore geometry and selectivity, we plotted permselectivity against pore size and length at various C_{high} concentrations (Fig. 6). Smaller pore sizes led to much higher selectivity, and this effect was more pronounced at higher concentrations (Fig. 6a). This highlights the sensitivity of the pore size as a parameter; an increase in just 5 nm could mean a 30% selectivity decrease for concentrations above 100 mM. It also shows that small pores can be selective even at high concentrations. This result underscores the importance of precise fabrication of NFMs, as a wider pore size distribution can have negative impacts on selectivity, which could be a challenge for large-scale (m^2) fabrication. To reiterate, pores smaller than 3 nm were not modeled because the continuum assumption becomes questionable at those scales. In addition, pores smaller than 1 nm are expected to lose the advantage of enhancing transmembrane transport since, at that level of confinement, the Stern layer covers the majority of the pore, where the water's viscosity greatly increases and the diffusion coefficient of the ions decreases [56,69,70].

Fig. 6b shows the effect of pore length on selectivity. An increase in pore length from a couple tens of nm to a couple hundreds of nm can substantially improve the selectivity, while selectivity is not very sensitive to pore length in the micrometer range. Based on our results, a minimum length is thus required, though pore lengths above several μms are unnecessary for selective AAO IEMs.

On the other hand, 2D or atomically thin materials have also been shown to be selective up to over 80% [44]. To explain this occurrence, we made a separate model in COMSOL Multiphysics, which included not only the nanopore itself, but also the surface of the membrane. The result (Figs. S14 and S15) showed that for longer pores ($L \gg R_p$), the surface doesn't affect selectivity; but for short or 2D pores, the surface itself has a significant effect. Therefore, we attribute the selectivity of 2D materials (typically graphene) to EDL overlap, their large surface potential, and the surface itself, which is more prominent since the pore density is typically lower. For materials with a lower surface potential and high pore density, however, 2D materials are expected to remain selective only when there is EDL overlap, which is already at sub-nanometer level for concentrations above 100 mM (**Equation (1)**).

To further understand the effect of surface potential and electrolyte concentration, we plotted the effect of the changing ζ-potential (Fig. 7a) and electrolyte concentration (Fig. 7b) on selectivity.

Fig. 7a shows that selectivity was strongly enhanced for higher ζ-potential. The ζ-potential can be viewed as a material property, but it is also strongly affected by the pH. Therefore, 0 potential can also be interpreted as the isoelectric point, the higher potentials as the effect of a more acidic pH and vice versa. Actual potential values would naturally depend on material, structure, and environment. In addition, this is also a highly sensitive parameter (for direct comparison with pore size, see Fig. S16), so the surface potential or choice of material represents an important lever in achieving ion selectivity.

Surface potential could also be externally altered by applying a potential to the membrane itself [71–73]. This can be particularly beneficial, for example to switch between anion and cation selectivity or in electrolysis applications where the membrane can be placed in contact with one of the electrodes. In the latter, a small overpotential can be required to greatly improve membrane selectivity, but it is only feasible if Faradaic reactions that occur on the surface of the NFM can be prevented. Fortunately, these materials are often dielectric, they exhibit low catalytic activity, and the required potential window to make the membrane selective is quite low. However, for applications where stacks of membranes are used, such as RED, this approach may be unsuitable since each membrane would need its own source of external charge and likely a reference electrode, which is impractical.

The final parameter studied was the concentration ratio. Fig. 7b displays the simulations performed for a pore with a 7-nm diameter and a 40-mV surface potential for different C_{high}:C_{low} ratios. Naturally, the selectivity was highest for a low electrolyte concentration (low C_{high}) and for a higher ratio (which implies low C_{low}). The impact of the concentration ratio was more pronounced at higher concentrations. To study which side (C_{low} or C_{high}) had a larger impact on selectivity, we plotted the apparent permselectivity against the arithmetic, the harmonic, and the geometric average of C_{high} and C_{low} (Fig. S17). For the geometric average, the lines for all concentration ratios were almost coincident, indicating that the geometric average in electrolyte concentration is determining the selectivity. Geometric average is always lower than (or equal to) arithmetic average, which means the lower side has a quadratically larger impact on selectivity than the higher concentration side. This property makes these membranes a good option for applications where the electrolyte concentration is very high on one side and very low on the other side, such as RED.

In order to look into their peak performance, we simulated a membrane with 3-nm pores and 5-μm length and considered one scenario in which the membrane had 40 mV of ζ-potential and one with 100 mV. We conservatively assumed that the membrane was being used for power generation through a salinity gradient, between a river with a 17-mM salt concentration and seawater (0.6 M) (see Fig. S18). The results

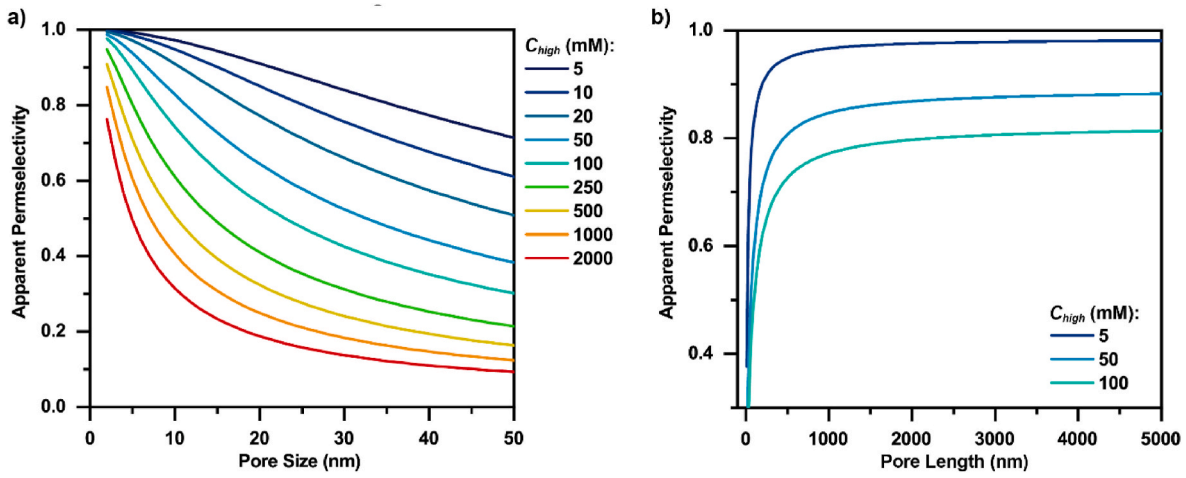

Fig. 6. a) Effect of pore size vs. different concentrations is shown. b) Effect of pore length on apparent selectivity is shown. C_{high}:C_{low} ratio is fixed at 5.

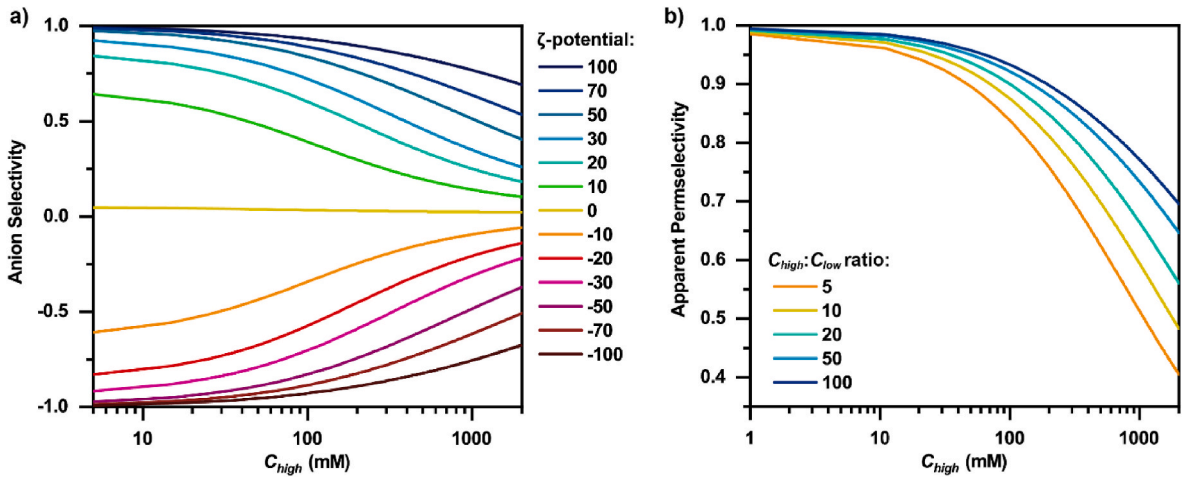

Fig. 7. Simulations performed for a 6-nm pore with boundary conditions of 40-mV surface potential. a) Effect of the surface potential boundary conditions on permselectivity is shown, with a negative "anion selectivity" representing selectivity toward cations. b) Effect of the ratio between C_{high} and C_{low} on permselectivity is shown.

show that this membrane would have a 97.7% selectivity at 100 mV and 93.3% with 40 mV of surface potential. The result with 100-mV surface potential surpassed many of the polymeric IEMs used for this application; these values can be even higher since this simulation was done with a ratio C_{high}:C_{low} of 35 while in practical RED processes, it can be as high as 500. We want to highlight that this prediction is based on the space-charge model, which has not yet been experimentally proven to accurately predict the selectivity for membranes with a pore size as low as 3–5 nm. Experimental proof of this prediction would be highly valued.

In terms of conductivity, the currently commercially available NFM materials, do not perform well enough to compete with polymeric IEMs. The AAO membranes we tested experimentally, have at least a 100 Ω cm^2 ionic resistance when placed between two compartments with 0.1 M KCl. This is because the membrane thickness is not optimized and the effective porosity is very low – see Fig. 3b, many channels have a dead end. Laboratory-made NFMs in other works have shown ionic resistances as low as 1 Ω cm^2, which is lower than many polymeric IEMs [50,74,75].

In this work, we've shown that nanofluidic IEMs can act as a selective ion separator, reaffirming their potential for applications such as RED and electrolysis [35,51,76]. Anodized metal oxides can be fabricated with fine-tuned pore sizes and geometries, adaptable for different applications [77]. The inorganic nature of these materials also brings the advantage of no swelling. Swelling of polymeric IEMs can be a challenge when assembling a large stack of membranes, since it is dependent on ion concentration and temperature, among other parameters. Additionally, creating an ultrathin (5 μm or less) nanofluidic IEM can enhance ion conductivity without compromising selectivity. It would be insightful if these results were verified experimentally by creating membranes with different thicknesses (i.e. pore lengths).

On the other hand, the inorganic nature of the materials also means that these membranes can be extremely brittle, especially when ultrathin. This could pose practical and transportation challenges, therefore requiring the use of a support material. The chemical stability of AAO membranes is also very limited, especially at alkaline pH and in aqueous solutions. Over time, the pores become clogged due to formation of aluminium hydroxide. However, other materials, such as titanium, can also be anodized to create the same geometries in a controlled manner. Anodized metal oxides can be easily coated, for example with atomic layer deposition, electroless deposition, or simple functionalizations with organic acids to manipulate their chemical stability [77]. This can improve chemical stability and also change the material's surface potential to enhance selectivity. Anodized metal oxide membranes are currently commercially available exclusively in cm^2 scale. Their defect-free production in m^2 scale remains a major challenge. Other methods to produce materials with a dense array of cylindrical nanopores include plating polycarbonate membranes and synthesis of nanoporous silica films via sol-gel techniques [72,78,79].

Another challenge is related to the surface potential being affected by pH. Most materials have a negative surface potential at high pHs, thus making it very difficult to create anion-exchange membranes in highly alkaline environments, or cation-exchange membrane in acidic environments. Although this is not a problem for most RED processes, it can be relevant for electrocatalytic applications, such as CO_2 electrolysis or water electrolysis. In that case, the external charging can be used to circumvent loss of anion selectivity at high pH in electrolysis applications.

NFMs could also have an increased water and gas permeability due to their comparatively more open structure, which could compromise the energy efficiency in RED or induce gas crossover risks in electrolysis. However, the water transport through the AAO membranes was negligible in our experiments ($<10^{-12}$ m^2/s). For reference, we measured the water permeability of the Selemion AMV membrane at $(5 \pm 1)*10^{-10}$ m^2/s and $(2.2 \pm 0.3)*10^{-9}$ m^2/s for Zirfon Perl UTP500, which is close to other reported values in literature [65,80]. The extremely low water permeability of NFMs, despite the porous structure, is likely related to their low effective porosity. Other values in literature suggest that their water permeability is in the same order of magnitude [81], or slightly higher than of polymeric IEMs [82]. A more open and thinner NFM would likely enhance the water transport, and reduce the ionic resistance at the same time. Because the water transport is currently orders of magnitude lower than polymeric IEMs, there is room for increasing the effective porosity of NFMs.

This study has also reaffirmed that the space-charge model can predict the selectivity of the nanofluidic IEMs. We recommend that future models include finite ion size, as this can change the total concentration inside the nanopore, especially at larger concentrations. For very small pore sizes, they should also include a variable diffusion coefficient since it is known that in a nanoconfined fluid, the diffusion coefficient will be affected, especially when close to the pore walls [69,70]. The diffusion coefficient is of great importance when simulating the conductivity of the membranes. It is good practice to consider the Stern layer thickness, where virtually no ion transport occurs as described in Ref. [71]. For 2D materials or very short nanopores, the membrane surface should also be included for accurate simulations.

5. Conclusions

In this study, we tested commercial AAO membranes with different pore sizes on their functionality as IEMs. We measured the apparent permselectivity of the membranes by placing them between two compartments of different electrolyte concentrations and measuring the potential across the membrane. The results showed that up to electrolyte concentrations of ~0.15 vs. 0.75 M, the AAO membranes with ~7-nm pores had a selectivity above 90%, which is comparable to polymeric IEMs. To our knowledge, this is the highest reported selectivity for nanofluidic IEMs in the literature, thus proving the concept's potential. Anisotropic membranes with a thin selective layer of 3-nm and 5-nm pores did not achieve high selectivities. Further, we used the space-charge model to explain these results and gain further understanding on how pore geometry can be modified to optimize selectivity.

Our simulations showed that pore size and surface potential are the most sensitive parameters for selectivity. Smaller nanopores can potentially achieve even higher selectivities, especially if a material with a higher surface potential or ζ-potential is used. However, the ζ-potential is not only dependent on the material but on the environment and pH as well. The simulations also showed that a minimum pore length is necessary to achieve selectivity although increasing the pore length in the μm scale has no significant effect. The concentrations on the two sides of the membrane were also found to have a large impact on selectivity, with the geometric average between the two being the determining parameter for selectivity.

Although challenges still restrict large-scale fabrication and implementation of nanofluidic membranes, we have shown that these materials can act as selective IEMs. Ultimately, the development of nanofluidic membranes as a replacement of polymeric IEMs could improve the performance of many electrochemical membrane processes, ranging from RED to electrolysis.

CRediT authorship contribution statement

Kostadin V. Petrov: Conceptualization, Validation, Formal analysis, Investigation, Writing – Original draft, Visualization, Project administration. **Mark Mao:** Methodology, Investigation. **Albert Santoso:** Investigation. **Ilya I. Ryzhkov:** Methodology, Software, Writing – Review & editing. **David A. Vermaas:** Supervision, Writing – Review & editing, Project administration, Funding acquisition.

Declaration of competing interest

The authors declare that they have no known competing financial interests or personal relationships that could have appeared to influence the work reported in this paper.

Data availability

Data will be made available on request.

Acknowledgements

This work is part of the research programme Towards large-scale electroconversion systems (TOeLS) financed by Shell and the Top-sectors Chemistry, HTSM and Energy.

Appendix A. Supplementary data

Supplementary data to this article can be found online at https://doi.org/10.1016/j.memsci.2023.122156.

References

[1] J.R. Varcoe, P. Atanassov, D.R. Dekel, A.M. Herring, M.A. Hickner, P.A. Kohl, A. R. Kucernak, W.E. Mustain, K. Nijmeijer, K. Scott, T. Xu, L. Zhuang, Anion-exchange membranes in electrochemical energy systems, Energy Environ. Sci. 7 (2014) 3135–3191, https://doi.org/10.1039/C4EE01303D.
[2] R. Xia, S. Overa, F. Jiao, Emerging electrochemical processes to decarbonize the chemical industry, JACS Au 2 (2022) 1054–1070, https://doi.org/10.1021/jacsau.2c00138.
[3] T. Luo, S. Abdu, M. Wessling, Selectivity of ion exchange membranes: a review, J. Membr. Sci. 555 (2018) 429–454, https://doi.org/10.1016/j.memsci.2018.03.051.
[4] Chapter 4 - operating principle of electrodialysis and related processes, in: H.B. T.-M.S, T. Strathmann (Eds.), Ion-Exchange Membr. Sep. Process, Elsevier, 2004, pp. 147–225, https://doi.org/10.1016/S0927-5193(04)80035-4.
[5] V. Silva, E. Poiesz, P. van der Heijden, Industrial wastewater desalination using electrodialysis: evaluation and plant design, J. Appl. Electrochem. 43 (2013) 1057–1067, https://doi.org/10.1007/s10800-013-0551-4.
[6] H. Strathmann, Electrodialysis, a mature technology with a multitude of new applications, Desalination 264 (2010) 268–288, https://doi.org/10.1016/j.desal.2010.04.069.
[7] A. Oehmen, R. Viegas, S. Velizarov, M.A.M. Reis, J.G. Crespo, Removal of heavy metals from drinking water supplies through the ion exchange membrane bioreactor, Desalination 199 (2006) 405–407, https://doi.org/10.1016/j.desal.2006.03.091.
[8] E. Güler, R. Elizen, D.A. Vermaas, M. Saakes, K. Nijmeijer, Performance-determining membrane properties in reverse electrodialysis, J. Membr. Sci. 446 (2013) 266–276, https://doi.org/10.1016/j.memsci.2013.06.045.
[9] D.A. Vermaas, M. Saakes, K. Nijmeijer, Power generation using profiled membranes in reverse electrodialysis, J. Membr. Sci. 385–386 (2011) 234–242, https://doi.org/10.1016/j.memsci.2011.09.043.
[10] D.R. Dekel, Review of cell performance in anion exchange membrane fuel cells, J. Power Sources 375 (2018) 158–169, https://doi.org/10.1016/j.jpowsour.2017.07.117.
[11] K. Jiao, J. Xuan, Q. Du, Z. Bao, B. Xie, B. Wang, Y. Zhao, L. Fan, H. Wang, Z. Hou, S. Huo, N.P. Brandon, Y. Yin, M.D. Guiver, Designing the next generation of proton-exchange membrane fuel cells, Nature 595 (2021) 361–369, https://doi.org/10.1038/s41586-021-03482-7.
[12] B. Schwenzer, J. Zhang, S. Kim, L. Li, J. Liu, Z. Yang, Membrane development for vanadium redox flow batteries, ChemSusChem 4 (2011) 1388–1406, https://doi.org/10.1002/cssc.201100068.
[13] D. Chen, M.A. Hickner, E. Agar, E.C. Kumbur, Optimized anion exchange membranes for vanadium redox flow batteries, ACS Appl. Mater. Interfaces 5 (2013) 7559–7566, https://doi.org/10.1021/am401858r.
[14] S. Lakshmanan, T. Murugesan, The chlor-alkali process: work in progress, clean technol, Environ. Pol. 16 (2014) 225–234, https://doi.org/10.1007/s10098-013-0630-6.
[15] S.A. Grigoriev, V.N. Fateev, D.G. Bessarabov, P. Millet, Current status, research trends, and challenges in water electrolysis science and technology, Int. J. Hydrogen Energy 45 (2020) 26036–26058, https://doi.org/10.1016/j.ijhydene.2020.03.109.
[16] P. Fortin, T. Khoza, X. Cao, S.Y. Martinsen, A. Oyarce Barnett, S. Holdcroft, High-performance alkaline water electrolysis using Aemion™ anion exchange membranes, J. Power Sources 451 (2020), 227814, https://doi.org/10.1016/j.jpowsour.2020.227814.
[17] M.A. Blommaert, S. Subramanian, K. Yang, W.A. Smith, D.A. Vermaas, High indirect energy consumption in AEM-based CO2 electrolyzers demonstrates the potential of bipolar membranes, ACS Appl. Mater. Interfaces 14 (2022) 557–563, https://doi.org/10.1021/acsami.1c16513.
[18] T. Sata, G.N. Jones, Ion Exchange Membranes, The Royal Society of Chemistry, 2004, https://doi.org/10.1039/9781847551177.
[19] F.G. Donnan, Theorie der Membrangleichgewichte und Membranpotentiale bei Vorhandensein von nicht dialysierenden Elektrolyten. Ein Beitrag zur physikalisch-chemischen Physiologie, Zeitschrift Für Elektrochemie Und Angew. Phys. Chemie. 17 (1911) 572–581, https://doi.org/10.1002/bbpc.19110171405.
[20] G.E. Molau, Heterogeneous ion-exchange membranes, J. Membr. Sci. 8 (1981) 309–330, https://doi.org/10.1016/S0376-7388(00)82318-2.
[21] R.A. Tufa, M.A. Blommaert, D. Chanda, Q. Li, D.A. Vermaas, D. Aili, Bipolar membrane and interface materials for electrochemical energy systems, ACS Appl. Energy Mater. 4 (2021) 7419–7439, https://doi.org/10.1021/acsaem.1c01140.
[22] S.M. Dischinger, S. Gupta, B.M. Carter, D.J. Miller, Transport of neutral and charged solutes in imidazolium-functionalized poly(phenylene oxide) membranes for artificial photosynthesis, Ind. Eng. Chem. Res. 59 (2020) 5257–5266, https://doi.org/10.1021/acs.iecr.9b05628.
[23] I. Stenina, D. Golubenko, V. Nikonenko, A. Yaroslavtsev, Selectivity of transport processes in ion-exchange membranes: relationship with the structure and methods for its improvement, Int. J. Mol. Sci. 21 (2020), https://doi.org/10.3390/ijms21155517.
[24] A.H. Galama, J.W. Post, M.A. Cohen Stuart, P.M. Biesheuvel, Validity of the Boltzmann equation to describe Donnan equilibrium at the membrane–solution interface, J. Membr. Sci. 442 (2013) 131–139, https://doi.org/10.1016/j.memsci.2013.04.022.
[25] G.M. Geise, M.A. Hickner, B.E. Logan, Ionic resistance and permselectivity tradeoffs in anion exchange membranes, ACS Appl. Mater. Interfaces 5 (2013) 10294–10301, https://doi.org/10.1021/am403207w.

[26] R.S. Kingsbury, J. Wang, O. Coronell, Comparison of water and salt transport properties of ion exchange, reverse osmosis, and nanofiltration membranes for desalination and energy applications, J. Membr. Sci. 604 (2020), 117998, https://doi.org/10.1016/j.memsci.2020.117998.

[27] D. Kitto, J. Kamcev, The need for ion-exchange membranes with high charge densities, J. Membr. Sci. 677 (2023), 121608, https://doi.org/10.1016/j.memsci.2023.121608.

[28] A. Daniilidis, D.A. Vermaas, R. Herber, K. Nijmeijer, Experimentally obtainable energy from mixing river water, seawater or brines with reverse electrodialysis, Renew. Energy 64 (2014) 123–131, https://doi.org/10.1016/j.renene.2013.11.001.

[29] M.N.Z. Abidin, M.M. Nasef, J. Veerman, Towards the development of new generation of ion exchange membranes for reverse electrodialysis: a review, Desalination 537 (2022), 115854, https://doi.org/10.1016/j.desal.2022.115854.

[30] A.B. Yaroslavtsev, I.A. Stenina, Current progress in membranes for fuel cells and reverse electrodialysis, Mendeleev Commun. 31 (2021) 423–432, https://doi.org/10.1016/j.mencom.2021.07.001.

[31] L. Gubler, Membranes and separators for redox flow batteries, Curr. Opin. Electrochem. 18 (2019) 31–36, https://doi.org/10.1016/j.coelec.2019.08.007.

[32] C.A. Machado, G.O. Brown, R. Yang, T.E. Hopkins, J.G. Pribyl, T.H.I.I.I. Epps, Redox flow battery membranes: improving battery performance by leveraging structure–property relationships, ACS Energy Lett. 6 (2021) 158–176, https://doi.org/10.1021/acsenergylett.0c02205.

[33] D.A. Salvatore, C.M. Gabardo, A. Reyes, C.P. O'Brien, S. Holdcroft, P. Pintauro, B. Bahar, M. Hickner, C. Bae, D. Sinton, E.H. Sargent, C.P. Berlinguette, Designing anion exchange membranes for CO2 electrolysers, Nat. Energy 6 (2021) 339–348, https://doi.org/10.1038/s41560-020-00761-x.

[34] S. Garg, C.A. Giron Rodriguez, T.E. Rufford, J.R. Varcoe, B. Seger, How membrane characteristics influence the performance of CO2 and CO electrolysis, Energy Environ. Sci. 15 (2022) 4440–4469, https://doi.org/10.1039/D2EE01818G.

[35] Z. Zhang, L. Wen, L. Jiang, Nanofluidics for osmotic energy conversion, Nat. Rev. Mater. 6 (2021) 622–639, https://doi.org/10.1038/s41578-021-00300-4.

[36] G. Merle, M. Wessling, K. Nijmeijer, Anion exchange membranes for alkaline fuel cells: a review, J. Membr. Sci. 377 (2011) 1–35, https://doi.org/10.1016/j.memsci.2011.04.043.

[37] R. Ghalloussi, W. Garcia-Vasquez, L. Chaabane, L. Dammak, C. Larchet, S. V Deabate, E. Nevakshenova, V. Nikonenko, D. Grande, Ageing of ion-exchange membranes in electrodialysis: a structural and physicochemical investigation, J. Membr. Sci. 436 (2013) 68–78, https://doi.org/10.1016/j.memsci.2013.02.011.

[38] L. Wang, M.S.H. Boutilier, P.R. Kidambi, D. Jang, N.G. Hadjiconstantinou, R. Karnik, Fundamental transport mechanisms, fabrication and potential applications of nanoporous atomically thin membranes, Nat. Nanotechnol. 12 (2017) 509–522, https://doi.org/10.1038/nnano.2017.72.

[39] A. Kayvani Fard, G. McKay, A. Buekenhoudt, H. Al Sulaiti, F. Motmans, M. Khraisheh, M. Atieh, Inorganic membranes: preparation and application for water treatment and desalination, Materials 11 (2018) 74, https://doi.org/10.3390/ma11010074.

[40] R.C. Rollings, A.T. Kuan, J.A. Golovchenko, Ion selectivity of graphene nanopores, Nat. Commun. 7 (2016), 11408, https://doi.org/10.1038/ncomms11408.

[41] R. Ishimatsu, J. Kim, P. Jing, C.C. Striemer, D.Z. Fang, P.M. Fauchet, J.L. McGrath, S. Amemiya, Ion-selective permeability of an ultrathin nanoporous silicon membrane as probed by scanning electrochemical microscopy using micropipet-supported ITIES tips, Anal. Chem. 82 (2010) 7127–7134, https://doi.org/10.1021/ac1005052.

[42] K. Zhou, J.M. Perry, S.C. Jacobson, Transport and sensing in nanofluidic devices, Annu. Rev. Anal. Chem. 4 (2011) 321–341, https://doi.org/10.1146/annurev-anchem-061010-113938.

[43] I. Vlassiouk, T.R. Kozel, Z.S. Siwy, Biosensing with nanofluidic diodes, J. Am. Chem. Soc. 131 (2009) 8211–8220, https://doi.org/10.1021/ja901120f.

[44] M. Ghosh, K.F.A. Jorissen, J.A. Wood, R.G.H. Lammertink, Ion transport through perforated graphene, J. Phys. Chem. Lett. 9 (2018) 6339–6344, https://doi.org/10.1021/acs.jpclett.8b02771.

[45] D. Lebedev, G. Malyshev, I. Ryzhkov, A. Mozharov, K. Shugurov, V. Sharov, M. Panov, I. Tumkin, P. Afonicheva, A. Evstrapov, A. Bukatin, I. Mukhin, Focused ion beam milling based formation of nanochannels in silicon-glass microfluidic chips for the study of ion transport, Microfluid. Nanofluidics 25 (2021) 51, https://doi.org/10.1007/s10404-021-02450-x.

[46] K. Xiao, L. Chen, Z. Zhang, G. Xie, P. Li, X.-Y. Kong, L. Wen, L. Jiang, A tunable ionic diode based on a biomimetic structure-tailorable nanochannel, Angew. Chem. Int. Ed. 56 (2017) 8168–8172, https://doi.org/10.1002/anie.201704137.

[47] M. Ali, P. Ramirez, H.Q. Nguyen, S. Nasir, J. Cervera, S. Mafe, W. Ensinger, Single cigar-shaped nanopores functionalized with amphoteric amino acid chains: experimental and theoretical characterization, ACS Nano 6 (2012) 3631–3640, https://doi.org/10.1021/nn3010119.

[48] W. Lee, S.-J. Park, Porous anodic aluminum oxide: anodization and templated synthesis of functional nanostructures, Chem. Rev. 114 (2014) 7487–7556, https://doi.org/10.1021/cr500002z.

[49] A.P. Li, F. Müller, A. Birner, K. Nielsch, U. Gösele, Hexagonal pore arrays with a 50–420 nm interpore distance formed by self-organization in anodic alumina, J. Appl. Phys. 84 (1998) 6023–6026, https://doi.org/10.1063/1.368911.

[50] D.-K. Kim, C. Duan, Y.-F. Chen, A. Majumdar, Power generation from concentration gradient by reverse electrodialysis in ion-selective nanochannels, Microfluid. Nanofluidics 9 (2010) 1215–1224, https://doi.org/10.1007/s10404-010-0641-0.

[51] J. Kim, S.J. Kim, D.-K. Kim, Energy harvesting from salinity gradient by reverse electrodialysis with anodic alumina nanopores, Energy 51 (2013) 413–421, https://doi.org/10.1016/j.energy.2013.01.019.

[52] Y. Lee, H.J. Kim, D.-K. Kim, Power generation from concentration gradient by reverse electrodialysis in anisotropic nanoporous anodic aluminum oxide membranes, Energies 13 (2020), https://doi.org/10.3390/en13040904.

[53] I.I. Ryzhkov, D. V Lebedev, V.S. Solodovnichenko, A. V Minakov, M.M. Simunin, On the origin of membrane potential in membranes with polarizable nanopores, J. Membr. Sci. 549 (2018) 616–630, https://doi.org/10.1016/j.memsci.2017.11.073.

[54] O. Stern, Zur THEORIE DER ELEKTROLYTISCHEN DOPPELSCHICHT, Zeitschrift Für Elektrochemie Und Angew. Phys. Chemie. 30 (1924) 508–516, https://doi.org/10.1002/bbpc.192400182.

[55] M.J. Braus, The Theory of Electrolytes. I. Freezing Point Depression and Related Phenomena, (Debye & Hückel, 1923), 2019.

[56] L. Bocquet, E. Charlaix, Nanofluidics, from bulk to interfaces, Chem. Soc. Rev. 39 (2010) 1073–1095, https://doi.org/10.1039/B909366B.

[57] A.R. Poggioli, A. Siria, L. Bocquet, Beyond the tradeoff: dynamic selectivity in ionic transport and current rectification, J. Phys. Chem. B 123 (2019) 1171–1185, https://doi.org/10.1021/acs.jpcb.8b11202.

[58] 3 - electric double layers, in: J.B.T.-F. of I., C.S. Lyklema (Eds.), Solid-Liquid Interfaces, Academic Press, 1995, pp. 3–232, https://doi.org/10.1016/S1874-5679(06)80006-1.

[59] J.L. Reyes Bahena, A. Robledo Cabrera, A. López Valdivieso, R. Herrera Urbina, Fluoride adsorption onto α-Al2O3 and its effect on the zeta potential at the alumina–aqueous electrolyte interface, Separ. Sci. Technol. 37 (2002) 1973–1987, https://doi.org/10.1081/SS-120003055.

[60] H.-J. Butt, K. Graf, M. Kappl, The electric double layer, Phys. Chem. Interfaces (2003) 42–56, https://doi.org/10.1002/3527602313.ch4.

[61] F.A. Morrison, J.F. Osterle, Electrokinetic energy conversion in ultrafine capillaries, J. Chem. Phys. 43 (1965) 2111–2115, https://doi.org/10.1063/1.1697081.

[62] J.H. Masliyah, S. Bhattacharjee, Numerical simulation of electrokinetic phenomena, in: Electrokinet, Colloid Transp. Phenom., 2006, pp. 537–611, https://doi.org/10.1002/0471799742.ch14.

[63] I.I. Ryzhkov, A.S. Vyatkin, E. V Mikhlina, Modelling of conductive nanoporous membranes with switchable ionic selectivity, Membr. Membr. Technol. 2 (2020) 10–19, https://doi.org/10.1134/S2517751620010072.

[64] R. Hartkamp, A.-L. Biance, L. Fu, J.-F. Dufrêche, O. Bonhomme, L. Joly, Measuring surface charge: why experimental characterization and molecular modeling should be coupled, Curr. Opin. Colloid Interface Sci. 37 (2018) 101–114, https://doi.org/10.1016/j.cocis.2018.08.001.

[65] J. Veerman, R.M. de Jong, M. Saakes, S.J. Metz, G.J. Harmsen, Reverse electrodialysis: comparison of six commercial membrane pairs on the thermodynamic efficiency and power density, J. Membr. Sci. 343 (2009) 7–15, https://doi.org/10.1016/j.memsci.2009.05.047.

[66] Z. Liu, H. Yang, R. Kutz, R.I. Masel, CO $_2$ electrolysis to CO and O $_2$ at high selectivity, stability and efficiency using sustainion membranes, J. Electrochem. Soc. 165 (2018) J3371–J3377, https://doi.org/10.1149/2.0501815jes.

[67] S. Novak, M. Kalin, The effect of pH on the wear of water-lubricated alumina and zirconia ceramics, Tribol. Lett. 17 (2004) 727–732, https://doi.org/10.1007/s11249-004-8080-2.

[68] R. Choudhary, D. Khurana, A. Kumar, S. Subudhi, Stability analysis of Al2O3/water nanofluids, J. Exp. Nanosci. 12 (2017) 140–151, https://doi.org/10.1080/17458080.2017.1285445.

[69] M.F. Döpke, R. Hartkamp, The importance of specifically adsorbed ions for electrokinetic phenomena: bridging the gap between experiments and MD simulations, J. Chem. Phys. 154 (2021), 94701, https://doi.org/10.1063/5.0038161.

[70] R. Hartkamp, B. Siboulet, J.-F. Dufrêche, B. Coasne, Ion-specific adsorption and electroosmosis in charged amorphous porous silica, Phys. Chem. Chem. Phys. 17 (2015) 24683–24695, https://doi.org/10.1039/C5CP03818A.

[71] I.I. Ryzhkov, M.A. Shchurkina, E. V Mikhlina, M.M. Simunin, I. V Nemtsev, Switchable ionic selectivity of membranes with electrically conductive surface: theory and experiment, Electrochim. Acta 375 (2021), 137970, https://doi.org/10.1016/j.electacta.2021.137970.

[72] M. Nishizawa, V.P. Menon, C.R. Martin, Metal nanotubule membranes with electrochemically switchable ion-transport selectivity, Science 268 (1995) 700–702, https://doi.org/10.1126/science.268.5211.700.

[73] A.A. Kapitonov, I.I. Ryzhkov, Modelling the performance of electrically conductive nanofiltration membranes, Membranes 13 (2023), https://doi.org/10.3390/membranes13060596.

[74] A. Aixalà-Perelló, A. Pedico, M. Laurenti, E. Fontananova, S. Bocchini, I.V. Ferrari, A. Lamberti, Scalable and highly selective graphene-based ion-exchange membranes with tunable permselectivity, Npj 2D Mater, Appl 7 (2023) 46, https://doi.org/10.1038/s41699-023-00399-9.

[75] Z. Zhang, S. Yang, P. Zhang, J. Zhang, G. Chen, X. Feng, Mechanically strong MXene/Kevlar nanofiber composite membranes as high-performance nanofluidic osmotic power generators, Nat. Commun. 10 (2019) 2920, https://doi.org/10.1038/s41467-019-10885-8.

[76] L. Cao, W. Guo, W. Ma, L. Wang, F. Xia, S. Wang, Y. Wang, L. Jiang, D. Zhu, Towards understanding the nanofluidic reverse electrodialysis system: well matched charge selectivity and ionic composition, Energy Environ. Sci. 4 (2011) 2259–2266, https://doi.org/10.1039/C1EE01088C.

[77] A.M. Md Jani, D. Losic, N.H. Voelcker, Nanoporous anodic aluminium oxide: advances in surface engineering and emerging applications, Prog. Mater. Sci. 58 (2013) 636–704, https://doi.org/10.1016/j.pmatsci.2013.01.002.
[78] T. Al-Harbi, F. Al-Hazmi, W.E. Mahmoud, Synthesis and characterization of nanoporous silica film via non-surfactant template sol–gel technique, Superlattice. Microst. 52 (2012) 643–647, https://doi.org/10.1016/j.spmi.2012.06.025.
[79] D. Zhao, J. Feng, Q. Huo, N. Melosh, G.H. Fredrickson, B.F. Chmelka, G.D. Stucky, Triblock copolymer syntheses of mesoporous silica with periodic 50 to 300 angstrom pores, Science 279 (1998) 548–552, https://doi.org/10.1126/science.279.5350.548.
[80] J. Schaep, C. Vandecasteele, R. Leysen, W. Doyen, Salt retention of Zirfon® membranes, Sep. Purif. Technol. 14 (1998) 127–131, https://doi.org/10.1016/S1383-5866(98)00067-7.
[81] D.I. Petukhov, D.A. Buldakov, A.A. Tishkin, A. V Lukashin, A.A. Eliseev, Liquid permeation and chemical stability of anodic alumina membranes, Beilstein J. Nanotechnol. 8 (2017) 561–570, https://doi.org/10.3762/bjnano.8.60.
[82] S.W. Lee, H. Shang, R.T. Haasch, V. Petrova, G.U. Lee, Transport and functional behaviour of poly(ethylene glycol)-modified nanoporous alumina membranes, Nanotechnology 16 (2005) 1335–1340, https://doi.org/10.1088/0957-4484/16/8/059.